THE JOURNAL OF PHYSICAL CHEMISTRY C

Article

pubs.acs.org/JPCC

# Mask-Assisted Seeded Growth of Segmented Metallic Heteronanostructures

Cameron C. Crane,[†] Jing Tao,[‡] Feng Wang,[†] Yimei Zhu,[‡] and Jingyi Chen*[,†]

[†]Department of Chemistry and Biochemistry, University of Arkansas, Fayetteville, Arkansas 72701, United States

[‡]Condensed Matter Physics and Materials Science Department, Brookhaven National Laboratory, Upton, New York 11973, United States

Supporting Information

**ABSTRACT:** Controlling the deposition of exotic metals in the seeded growth of multimetal nanostructures is challenging. This work describes a seeded growth method assisted by a mask for synthesis of segmented binary or ternary metal nanostructures. Silica is used as a mask to partially block the surface of a seed and a second metal is subsequently deposited on the exposed area, forming a bimetallic heterodimer. The initial demonstration was carried out on a Au seed, followed by deposition of Pd or Pt on the seed. It was found that Pd tended to spread out laterally on the seed while Pt inclined to grow vertically into branched topology on Au. Without removal of the $SiO_2$ mask, Pt could be further deposited on the unblocked Pd of the Pd−Au dimer to form a Pt−Pd−Au trimer. Mask-assisted seeded growth provides a general strategy to construct segmented metallic nanoarchitectures.

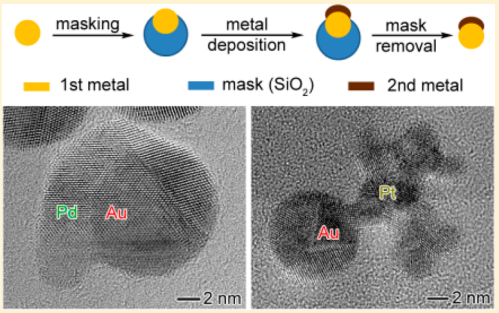


## INTRODUCTION

Heterostructures of two or more metals with interfaces at the nanoscale is of particular significance because they exhibit unique properties and multifunctions distinctly different from the individual components.[1−4] The diverse surface chemistry of these heteronanostructures enables new applications that are not possible with each component alone. For example, multisegmented metal nanorods have been demonstrated for applications in synergistic heterogeneous catalysis,[5,6] self-electrophoretic nanomotors/nanobatteries,[7,8] multifunctional biomedicine,[9,10] and multiplexed detections.[11,12] To fabricate the heteronanostructures, sequential electrochemical deposition of metal ions into templates has been the most common method since the 1990s.[13,14] In this approach, commercially available alumina or polycarbonate membranes with uniform pores are often used as templates, yielding segmented metal rods.[15] This method could be further extended to selective growth of additional metals within the templates in solution after the initial electrochemical deposition of rod-shaped seeds.[16,17] To generate heterostructures with other configurations, cost-intensive and time-consuming lithography techniques are usually required.[18] In this work, a site-selective seeded growth method, termed mask-assisted seeded growth (MASG), is developed to expand the library of metal heterostructures with complex nanoarchitectures.

Seeded growth has emerged as a compelling method to create a wide variety of novel metal nanostructures.[19−24] Conditions that yield heteronanostructures depend on a number of factors such as the structural characteristics of constituent components, the reduction kinetics of metal precursors, and the capping agents. For example, a high degree of lattice mismatch between the seed and the second metal prevents conformal growth of core@shell structures and yields heteronanostructures of Au on $CoPt_3$,[25] Au rods on Pt cubes,[21] and Cu on Au.[24] Controlling the reduction kinetics can selectively direct the nucleation and subsequent growth of the second metal on the seed to form dimers of Au on Pd[26] or other nonconformal structures such as Ag/Au on Pd cubes[27,28] and Ag on Au nanorods.[29] On the other hand, blocking specific facets of the seeds by capping agents could lead to the growth of Rh on Pd heterostructures.[30] Despite these advances, optimization of the growth conditions is largely material-specific, and it is beneficial to develop a general approach for the synthesis of multicomponent heteronanostructures.

In this work, the MASG method uses $SiO_2$ as a mask in seeded growth to partially block the surface of the seed and thus direct the deposition of exotic metals on the exposed surface of the seed, forming heteronanostructures. The asymmetric coating of $SiO_2$ was demonstrated in the classical Stöber synthesis by using a polymeric ligand to partially block the diffusion of the sol−gel precursor to reach the surface of the nanoparticle.[31] However, this method is only suitable for water-soluble nanoparticles. To overcome this limitation, the water-in-oil (W/O) microemulsion method is used to form the $SiO_2$ mask. Unlike the classical Stöber synthesis of $SiO_2$ coating,[31−34] the W/O microemulsion confines the sol−gel condensation within the water droplets in bulk oil, particularly useful for the formation of $SiO_2$ coating on nanoparticles suspended in

**Received:** September 17, 2014
**Revised:** November 4, 2014
**Published:** November 10, 2014

   dx.doi.org/10.1021/jp5094433 | J. Phys. Chem. C 2014, 118, 28134−28142

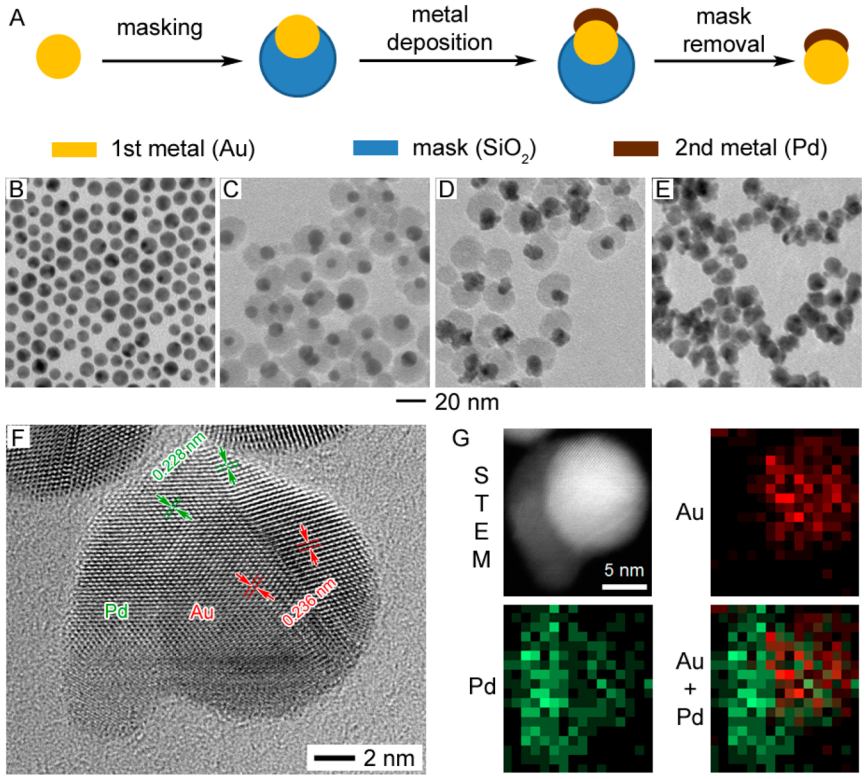


**Figure 1.** (A) Schematic illustration of the MASG method for synthesis of metallic heteronanostructures. TEM characterization of products from each step in the process is shown for Pd–Au as a demonstration: (B) Au spherical nanoparticles with a mean diameter of 9.7 ± 1.3 nm, (C) Au–$SiO_2$ dumbbell nanoparticles, (D) Pd–Au–$SiO_2$ nanoparticles, and (E) Pd–Au heterodimers. TEM characterization of an individual Pd–Au heterodimer is also shown: (F) HRTEM image and (G) HAADF-STEM image and EDX elemental mapping.

hydrophobic solvents.[35] By reducing the concentration of sol–gel precursor in the W/O microemulsion, phase separation between the surface ligand and hydrolyzed precursor is created on the particle surface, leading to partial condensation of $SiO_2$ on individual Au nanospheres to yield Au–$SiO_2$ dumbbell structures. Sequential reduction of Pd and Pt precursors on these dumbbell structures generates heterodimers of Pd–Au and Pt–Au and more complex Pt–Pd–Au heterotrimers. The reaction mechanisms of the microemulsion for preparation of Au–$SiO_2$ dumbbells and their subsequent use for synthesis of heteronanostructures are elucidated. These heteronanostructures exhibit tunable optical properties in the visible region that are markedly different from those of the individual components.

## EXPERIMENTAL SECTION

**Chemicals.** Hydrogen tetrachloroaurate trihydrate ($HAuCl_4 \cdot 3H_2O$, 99.99%), potassium tetrachloroplatinate ($K_2PtCl_4$, 99.9%), potassium tetrachloropalladate ($K_2PdCl_4$, 99.9%), and ammonium hydroxide (28–30% $NH_3 \cdot H_2O$) were purchased from Alfa Aesar. Tetradecylamine (TDA, >95%) was purchased from TCI. Tetraethoxysilane (TEOS, 98%), poly(oxyethylene) nonylphenyl ether (Igepal CO-520), and poly(vinylpyrrolidone) (PVP, MW = 55 000) were purchased from Sigma-Aldrich. Cyclohexane (ACS-grade) was purchased from EMD. All chemicals were used as received unless specified otherwise.

**Synthesis of Au–$SiO_2$ Dumbbells.** Au–$SiO_2$ dumbbells were synthesized by controlling the hydrolysis and condensation of the $SiO_2$ precursor during the coating process by use of W/O microemulsions. Initially, 10-nm Au nanoparticles were prepared by reducing $HAuCl_4 \cdot 3H_2O$ (19.7 mg, 0.05 mmol) in 5 g of TDA at 160 °C for 20 min under argon. After the reaction, the product was cooled to 100 °C and purified with toluene and ethanol to remove unreacted precursor and excess TDA. The Au nanoparticles were then dispersed in cyclohexane for $SiO_2$ coating in W/O microemulsions. In a typical procedure, 1 mL of 200 nM Au nanoparticles was added to the mixture of 0.14 M Igepal CO-520 in 40 mL of cyclohexane in a round-bottom flask equipped with a magnetic stirring bar. Various amounts of TEOS (20–200 $\mu$L) were added to the reaction mixture and allowed to mix for 30 min before the addition of 0.280 mL of $NH_3 \cdot H_2O$. The Au–$SiO_2$ dumbbell structures were formed when less than 50 $\mu$L of TEOS was used. The reaction was allowed to proceed for 48 h and stopped by addition of ethanol to interrupt the emulsion. The product was washed by ethanol and dispersed in 18 MΩ $H_2O$ for future use.

**Synthesis of Pd–Au Dimers.** The Pd–Au dimers were synthesized by reducing the Pd precursor in the presence of Au–$SiO_2$ dumbbells by use of ascorbic acid. In a typical procedure, 8 mL of $K_2PdCl_4$ was added, at a rate of 0.1 mL/min, to a 5 mL aqueous solution containing Au–$SiO_2$ dumbbells (~15 pmol) and PVP (1 mg/mL) at room temperature. Final concentrations of $K_2PdCl_4$ (0.06, 0.2, and 0.35 mM) in the reactions were used to yield Pd depositions with different thicknesses of ~4, ~7, and ~10 nm, respectively. The molar ratio of ascorbic acid to $K_2PdCl_4$ was kept at 10:1 for all three reactions. The product was washed by ethanol and dispersed in 18 MΩ $H_2O$. The $SiO_2$ component was then dissolved by mixing the Pd–Au–$SiO_2$ particles overnight in an aqueous solution containing excess NaOH and PVP (10 mg/


dx.doi.org/10.1021/jp5094433 | J. Phys. Chem. C 2014, 118, 28134–28142

mL). The product was washed with water and dispersed in 18 MΩ $H_2O$.

The thickness ($x_{Pd}$) of Pd deposition was estimated by use of a crude model that approximates the Pd layer as a semispherical shell interfacing with a spherical Au core. The radius of the semishell ($r_{Pd}$) can be derived from the average volume of Pd (cubic nanometers per particle): $V_{Pd} = {}^1/_2({}^4/_3\pi r_{Pd}{}^3 - {}^4/_3\pi r_{Au}{}^3)$, where $r_{Au}$ is the radius of the Au core that can be measured from the transmission electron microscopic (TEM) image. The $V_{Pd}$ was obtained from $V_{Pd}/V_{Au} = C_{Pd}a_{Pd}{}^3/C_{Au}a_{Au}{}^3$, where $V_{Au}$ is the average volume of Au (cubic nanometers per particle) when a spherical shape is assumed ($V_{Au} = {}^4/_3\pi r_{Au}{}^3$); $C_{Pd}$ and $C_{Au}$ are the concentration of Pd and Au (moles per liter), respectively, which can be measured from the bulk sample; and $a_{Pd}$ and $a_{Au}$ are the lattice constants of Pd and Au (nanometers), respectively. The difference of $r_{Pd}$ and $r_{Au}$ gives the thickness of the Pd semishell: $x_{Pd} = r_{Pd} - r_{Au}$.

**Synthesis of Pt–Au Dimers.** The procedure for Pt–Au dimers was the same as that for Pd–Au dimers described above, except that $K_2PtCl_4$ was used as the Pt precursor and the final concentration of Pt in the reaction solution was 2.4 mM.

**Synthesis of Pt–Pd–Au Trimers.** The Pt–Pd–Au trimers were synthesized by a similar procedure as that for Pt–Au dimers, except that Au–$SiO_2$ was replaced by the presynthesized Pd–Au–$SiO_2$ described above.

## RESULTS

The MASG method has been demonstrated to synthesize bimetallic and trimetallic heteronanostructures. Figure 1A illustrates the general strategy of the MASG method, using a Au seed and a second metal Pd as an example to create a heterodimer. This method involves $SiO_2$ to mask one side of a spherical nanoparticle and expose the other side for deposition of successive metals. After deposition, the $SiO_2$ mask can be removed to yield heterodimers, trimers, or oligomers depending on the number of repeated depositions performed during the seeded growth. As an initial demonstration, Au and Pd were used as the seed and the second metal, respectively. The Au seeds prepared by reducing chloroauric acid in tetradecylamine were spherical nanoparticles with diameter 9.7 ± 1.3 nm (Figure 1B). High-resolution TEM (HRTEM) analysis shows that the Au seeds adopted decahedral geometry consisting of five tetrahedral subunits (Figure S1, Supporting Information). The subunits were bounded by {111} crystal faces, arranged along a 5-fold rotation axis along the [110] zone.[36] Silica was subsequently condensed on these seeds by a modified W/O microemulsion method to form Au–$SiO_2$ dumbbells (Figure 1C). The yield of dumbbells was close to 90%, with half the seed surface covered by $SiO_2$. These $SiO_2$-masked seeds were used for the deposition of Pd. Upon reduction of Pd precursors with ascorbic acid, Pd was selectively deposited on the unblocked Au surface of these dumbbells to generate heterostructures of Pd–Au–$SiO_2$ (Figure 1D). Removal of the $SiO_2$ mask yielded Pd–Au heterodimers (Figure 1E).

The Pd–Au dimers were further characterized by HRTEM, high-angle annular dark-field scanning transmission electron microscopy (HAADF-STEM), and energy-dispersive X-ray spectroscopy (EDX). The HRTEM image of individual Pd–Au dimers clearly shows that the two components were assembled into heterostructures (Figure 1F). The *Z*-contrast HAADF-STEM image and EDX mapping indicate that the dimer adopted a mushroom configuration with a Au spherical stem and a Pd cap (Figure 1G). Further analysis of the HRTEM image shows the continuation of lattice fringes from Au to Pd. The lattice spacing was measured to be 0.236 and 0.228 nm, corresponding to the spacing of {111} planes of Au and Pd, respectively. This result suggests epitaxial growth of Pd on the {111} facets of decahedral 5-fold twinned Au nanoparticles, in agreement with previous in situ TEM observations.[37] Without the $SiO_2$ mask, no Au–Pd dumbbells were found in the product under identical conditions (Figure S2, Supporting Information).

The growth of Pd on Au–$SiO_2$ dumbbells could be manipulated by varying the amount of Pd precursor introduced during deposition onto the Au–$SiO_2$ seeds. The amount of Au–$SiO_2$ seeds was kept constant, and the concentration of Au–$SiO_2$ was estimated from the extinction coefficient at 520 nm [$\varepsilon_{Au} = (1.55 \pm 0.01) \times 10^8$ $M^{-1}\cdot cm^{-1}$; Figure S3, Supporting Information]. To maintain the same reaction volume, different concentrations of $K_2PdCl_4$ were added to the reaction containing 15 pmol of Au-$SiO_2$ at a rate of 0.1 mL/min. Because the underpotential deposition of Pd on Au favors heterogeneous nucleation of Pd on Au over Pd on Pd,[38,39] Pd preferentially nucleates laterally on the Au surface to cover the entire area of the exposed Au prior to growth on newly deposited Pd. Increased concentration of $K_2PdCl_4$ from 0.06 to 0.20 to 0.35 mM resulted in thicker deposition of Pd, as shown in Figures 2A, 1D, and 2B, respectively. A crude model was

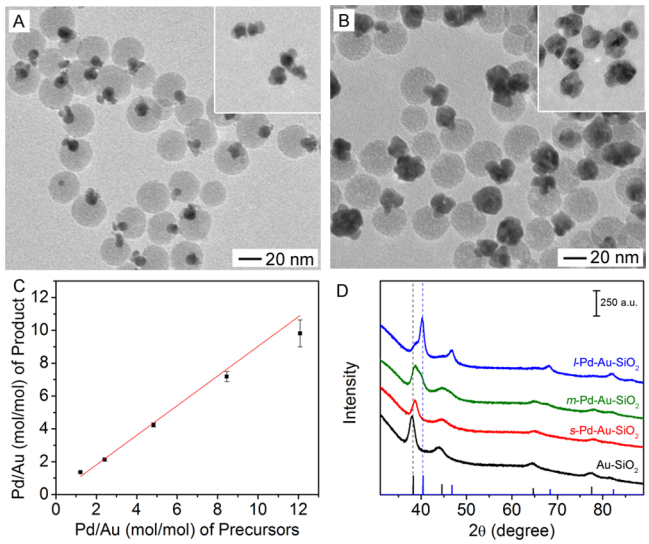


**Figure 2.** TEM characterization of Pd–Au–$SiO_2$ heteronanostructures with different thickness of Pd deposition: (A) 4 and (B) 10 nm. (Insets) Corresponding TEM images of Pd–Au heterodimers after the removal of silica. (C) Plot of relative quantities of Pd in the dimers versus that in the precursor. (D) XRD patterns of the Au-$SiO_2$ dumbbell nanoparticles (Au–$SiO_2$) and Pd–Au–$SiO_2$ heteronanostructures with Pd deposition thickness of 4, 7, and 10 nm, denoted as *s*-, *m*-, and *l*-Pd–Au–$SiO_2$, respectively.

established to calculate the deposition thickness of Pd by approximating the Pd layer as a semispherical shell interfacing with a spherical core of Au as described in the Experimental Section. The deposition thickness of Pd was estimated to be 4, 7, and 10 nm for the three samples, denoted as *s*-, *m*-, and *l*-Pd–Au–$SiO_2$, respectively.

Careful control of the reduction rate of the second metal is important to ensure heterogeneous nucleation and subsequent growth. A mild reduction of Pd was maintained for the


dx.doi.org/10.1021/jp5094433 | J. Phys. Chem. C 2014, 118, 28134–28142

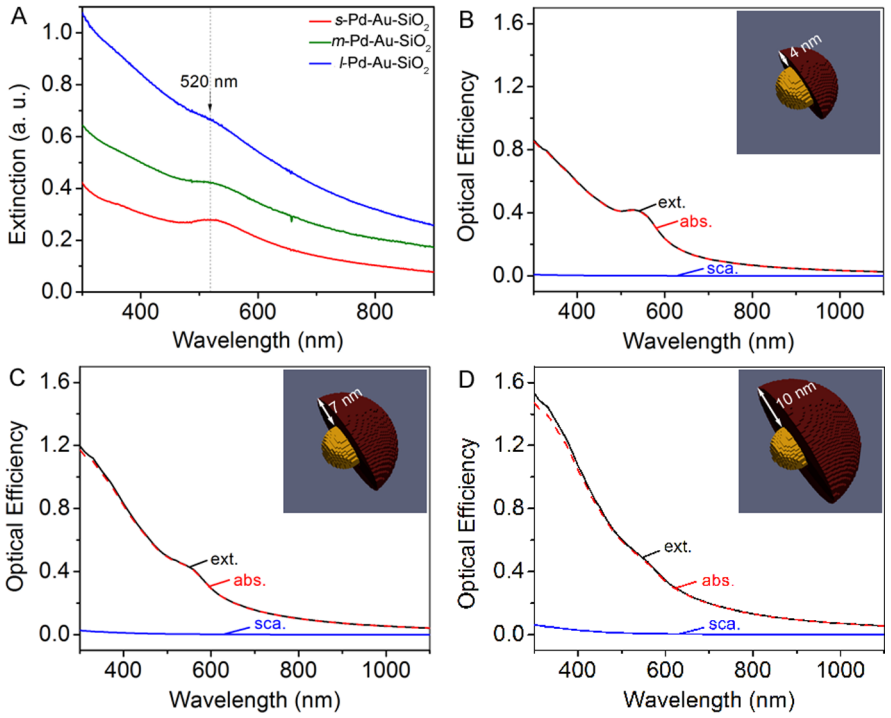


**Figure 3.** (A) UV−vis spectra of Pd−Au−$SiO_2$ heteronanostructures with Pd deposition thickness of 4, 7, and 10 nm on Au nanoparticles with a diameter of 9.7 ± 1.3 nm, denoted as *s*-, *m*-, and *l*-Pd-Au-$SiO_2$, respectively. (B−D) DDA simulation of the optical spectra of Pd−Au heterodimers with Pd deposition of 4, 7, and 10 nm on a Au nanosphere with a diameter of 10 nm, denoted as *s*-Pd−Au (B), *m*-Pd−Au (C), and *l*-Pd−Au (D), respectively. (Insets) Geometries of Pd−Au heterodimers used for the simulation.

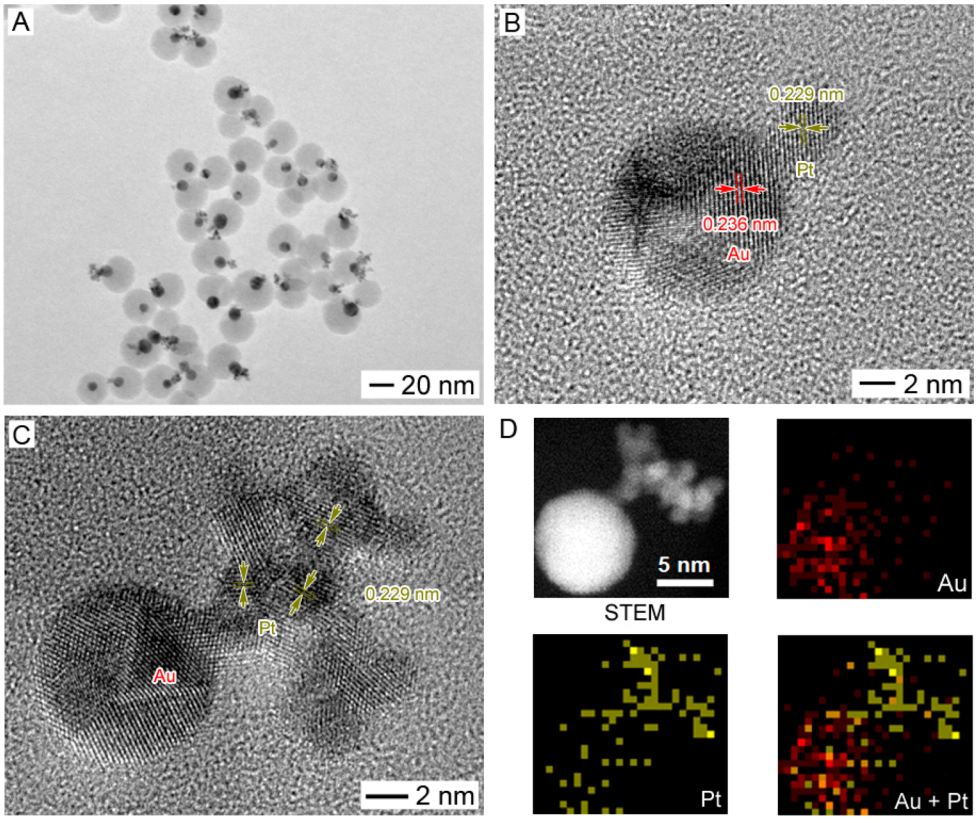


**Figure 4.** TEM characterization of Pt−Au−$SiO_2$ heterostructures: (A) overview image; (B, C) HRTEM of an individual particle; and (D) HAADF-STEM image and EDX elemental mapping.

deposition of Pd on Au by use of ascorbic acid as a reducing agent. The correlation between the amount of Pd formed and the amount of Pd precursor added was plotted in Figure 2C. In this study, the amount of ascorbic acid was in excess, 10:1 equiv


dx.doi.org/10.1021/jp5094433 | J. Phys. Chem. C 2014, 118, 28134−28142

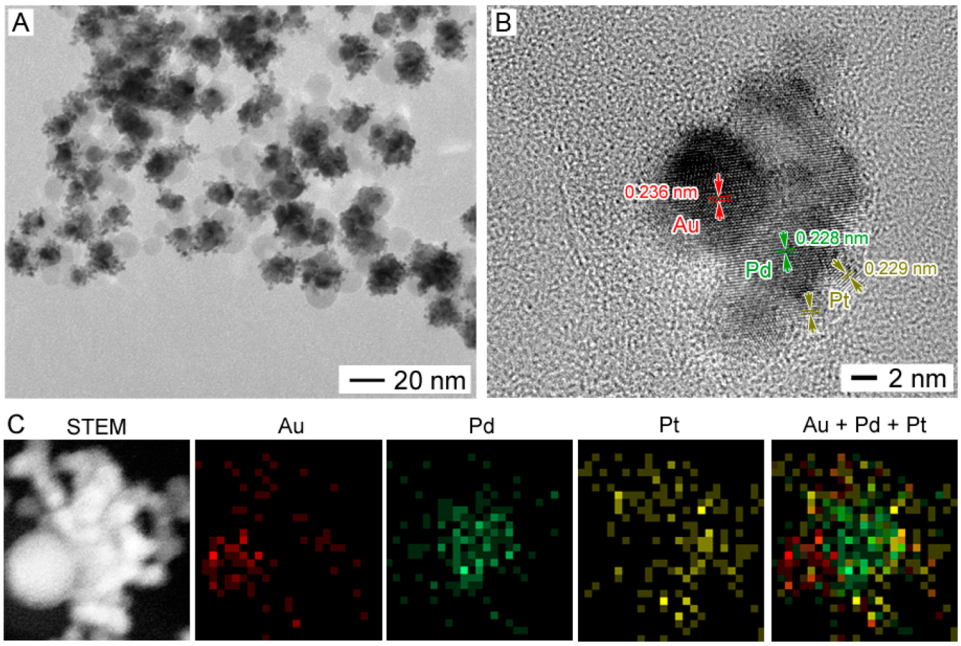


**Figure 5.** TEM characterization of Pt−Pd−Au−$SiO_2$ heteronanostructures: (A) overview image; (B) HRTEM of an individual particle; (C) HAADF-STEM image and EDX elemental mapping.

to the Pd precursor. The amount of deposited Pd on Au was linearly proportional to the amount of Pd precursor added to the reaction in the range of molar ratios of Pd to Au less than 10. The slope of the linear fitting curve was 0.90 ± 0.04, suggesting that nearly all the Pd precursor was reduced under these reaction conditions. The results of X-ray powder diffraction (XRD) also show an increase of the Pd-to-Au ratio denoted as *s*-, *m*-, and *l*-Pd−Au−$SiO_2$ by comparing the ratio of (111) peaks of Pd to Au in Figure 2D. Diffusion between the two metals at the interface may occur;[40] however, the rate could be rather slow at room temperature.[41,42]

The deposition of Pd on Au could be monitored by the change in optical properties of the resultant heteronanostructures. Figure 3A shows the UV−vis spectra of s-, m-, and l-Pd−Au−$SiO_2$. Due to the damping effects of Pd on the surface plasmon resonance of Au,[43] the extinction peak of Au nanoparticles at 520 nm was gradually flattened out as the deposition volume of Pd increased. The optical spectra were further simulated by the discrete dipole approximation (DDA) method,[44] based on our crudely modeled geometry shown in the insets of Figure 3B−D. Due to small size of the particles, light absorption dominated over scattering for their surface plasmon resonances. The simulated spectra matched well with the empirical extinction spectra, showing a decrease in extinction efficiency of Au at 520 nm after deposition of Pd, from 0.652 (Figure S4, Supporting Information) to 0.420 (Figure 3B), by about a third. As the size of Pd increases from $x_{Pd}$ of 4 to 7 to 10 nm, the extinction efficiency at 520 nm slightly increases from 0.420 to 0.470 to 0.550, respectively. The corresponding extinction cross sections of individual dimers increase from $0.75 \times 10^{-16}$ to $1.40 \times 10^{-16}$ to $2.50 \times 10^{-16}$ $m^2$. The optical spectra of another possible model of the Au−Pd dimer containing the same amount of Au and Pd by volume were also calculated. In this second model, the Au sphere is covered by a partial ellipsoid, as shown in Figure S5 (Supporting Information). The calculated spectra of the second model are very similar to those of the semispherical Pd shell model, suggesting that the optical spectra of the Au−Pd dimer are insensitive to certain details of the configuration such as the flat cutoff of a half-shell versus the curvature of an ellipsoid. By observing the change in the spectral shapes and intensity at 520 nm, the colorimetric method provides a simple and convenient means to track the deposition thickness of Pd in situ.

To further evaluate the versatility of the MASG method, Pt was examined as a second metal for deposition on the Au−$SiO_2$ dumbbells. Interestingly, Pt was deposited on Au as a dendritic configuration branching out vertically, as opposed to the lateral growth of Pd on Au (Figure 4). Further analysis of HRTEM images shows the lattice spacing was measured to be 0.236 and 0.228 nm, corresponding to the spacing of {111} planes of Au and Pt, respectively. It is suggested that Pt clusters could be deposited on Au seeds through either direct reduction or oriented attachment on the {111} facets of decahedral 5-fold twinned Au nanoparticles.[45,46] After the initial epitaxial growth of Pt on Au, growth of Pt on Pt is more favorable than that on Au, possibly due to the overpotential of Pt deposition on the Au surface.[47] The slow reduction kinetics promotes the growth of Pt along the ⟨111⟩ direction into branched structures. The HAADF-STEM image and EDX elemental mapping verified the composition of Au and Pt heterodimer structures.

The MASG method can be further extended to grow an additional component at a designated site of the heterodimers via the $SiO_2$ masking strategy. As a demonstration, Pt was added with ascorbic acid to the suspension of Pd−Au−$SiO_2$ heterostructures with Au protected by the $SiO_2$ coating. Dendritic Pt caps were formed on the Pd side of the Pd−Au dimers as shown in Figure 5, in contrast to equal deposition on both Pd and Au, which was observed on the unprotected dimers (Figure S6, Supporting Information). It is hard to differentiate Pd and Pt by comparing the lattice spacing of {111} facets because their lattice constants are almost identical (0.389 nm for Pd versus 0.392 for Pt).[48] However, the vertical growth pattern of Pt is distinctly different from the lateral one of Pd. From the HRTEM analysis, it was found that epitaxial


dx.doi.org/10.1021/jp5094433 | J. Phys. Chem. C 2014, 118, 28134−28142

growth was extended from Pd on Au{111} faces to Pt on Pd{111} faces of Pd–Au. The composition of Au, Pd, and Pt of individual heterotrimers was further confirmed by the HAADF-STEM image and EDX elemental mapping.

## DISCUSSION

The formation of metal–$SiO_2$ dumbbell nanoparticles is the key to the success of the MASG method. A high yield of Au–$SiO_2$ dumbbells was accomplished by a modified W/O microemulsion method. In a typical W/O microemulsion, the $SiO_2$ coating on a nanoparticle is formed by hydrolysis and condensation of TEOS within a micrometer- or nanometer-sized droplet that is generated in a homogeneous mixture of water, organic solvent (oil), and surfactant. The conventional method often results in core@shell structures with minimal inhomogeneity in the coating.[35] The modified W/O microemulsion was carried out by hydrolysis and condensation of TEOS on TDA-coated Au nanoparticles with ammonia in the presence of surfactant (Igepal CO-520) and organic solvent (cyclohexane). To increase the yield of Au–$SiO_2$ dumbbells, the concentration of TEOS was reduced to create phase separation between TDA and hydrolyzed TEOS on the surface of Au nanoparticles.

The mechanism based on phase separation in the W/O microemulsion is illustrated in Figure 6A. Initially, TDA ligands

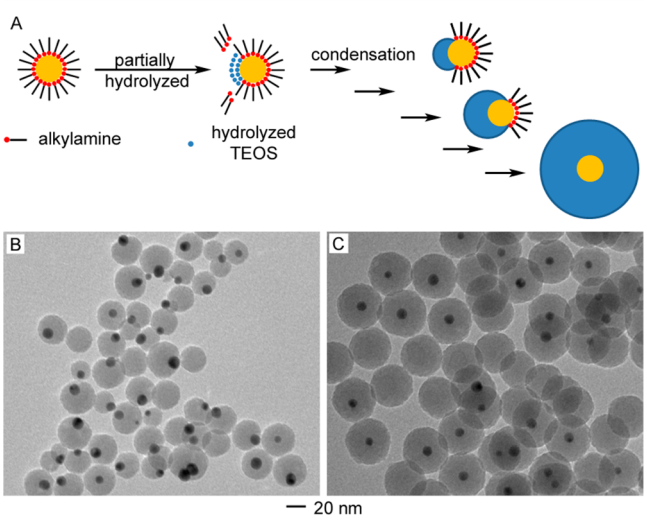


**Figure 6.** (A) Schematic illustration of the mechanism of silica coating via a microemulsion process. (B, C) TEM characterization of the corresponding samples in the proposed mechanism for two different concentrations of TEOS under identical reaction conditions: (B) at low concentration (3.4 mM) and (C) at high concentration (22.4 mM).

on the nanoparticles were partially replaced by the hydrolyzed TEOS, resulting in phase segregation of hydrophobic, aliphatic amine, and hydrophilic TEOS.[49] Further condensation of TEOS was limited to the hydrophilic portion of the particle surface, yielding dumbbell structures of Au–$SiO_2$ (Figure 6B). As the concentration of TEOS increases, more TDA ligands are substituted by the hydrolyzed TEOS, leading to a gradual expansion of TEOS to encompass the entire surface of the Au nanoparticles and thus further condensation to form a complete $SiO_2$ shell (Figure 6C). The resultant $SiO_2$ is porous, allowing small molecules to diffuse in and out more easily as compared to crystalline materials. For example, water can diffuse through the pores of $SiO_2$ to reach the surface of Au nanoparticles, resulting in a $SiO_2$ shell filled with water. If it is assumed that a simple mathematic average can be used to estimate the dielectric constant of a two-component mixture, the refractive index of porous $SiO_2$ surrounding Au nanoparticles can be shown to be very similar to that of toluene. This was confirmed by measuring the extinction spectra of Au nanoparticles in toluene and Au–$SiO_2$ in water. The spectra are very similar and consistent with our approximation (Figure S7, Supporting Information). Despite its porous nature, the $SiO_2$ mask can act as a protecting group and effectively reduce the surface accessibility of reactant molecules in a chemical reaction. To verify the protecting function of $SiO_2$, the reactivity of Au in the dumbbells and the core@shell structures was compared using two model reactions: an etching experiment using excess KCN and the reduction of *p*-nitrophenol by excess $NaBH_4$.

The reactivity of the Au cores in the dumbbells is markedly different from that of core@shell structures because $SiO_2$ coating largely blocks the diffusion of reactants. The etching of Au involves the use of KCN in aqueous solution as follows: $4Au + 8CN^- + O_2 + 2H_2O \rightarrow 4[Au(CN)_2]^- + 4OH^-$. The rate of the reaction is mainly limited by the diffusion of $CN^-$ through the pores of $SiO_2$ because the dissolved $O_2$ and water molecules have covered the surface of Au. As the size of Au nanoparticles decreases during the etching process, the extinction efficiency is reduced linearly while the cross section decreases exponentially (Figure S8, Supporting Information). The dissolution of Au could then be monitored by the diminished rate of extinction at 520 nm (Figure 7A). It was found that the etching rate of Au in the dumbbell particles was faster than that in the core@shell structures. In the case of core@shell structures, the etching rate was further slowed down after 10 min, possibly because the slower diffusion rate of the larger $[Au(CN)_2]^-$ anions further slows down the etching rate of Au. After dissolution of Au, the dumbbell particles yielded half shells of silica, while complete silica shells were found as the product for core@shell particles (Figure 7B,C). The slight change of $SiO_2$ morphology after etching could possibly be due to the structure reconstruction in the basic solution during the etching process.[50]

The accessibility of $SiO_2$-masked surface is much more difficult for the deposition of additional metals because the reduction typically involves two reactants: a relatively large anion of a transition metal complex and ascorbic acid. The assumption was examined by a model reaction involving two reactants: reduction of *p*-nitrophenol by excess $NaBH_4$. The same amounts of dumbbell particles and core@shell particles were used to catalyze the *p*-nitrophenol reduction. The reaction was monitored by decreased intensity of absorbance at 400 nm corresponding to the disappearance of *p*-nitrophenol (Figure 7D). The reduction could be treated as a pseudo-first-order reaction when $NaBH_4$ was in large excess.[51] The data were then plotted as first-order with respect to *p*-nitrophenol (Figure 7E). The rate constant of *p*-nitrophenol reduction on the dumbbell particles was found to be $(4.64 \pm 0.01) \times 10^{-3}$ $s^{-1}$, more than 10-fold faster compared to the core@shell structures $[(4.11 \pm 0.32) \times 10^{-4}$ $s^{-1}]$. In fact, *p*-nitrophenol reduction on the core@shell particles deviates from first-order kinetics, suggesting that the concentration of $NaBH_4$ is insufficient to assume pseudo-first-order reaction. This result, in turn, implies that the diffusion rates of reactants are significantly reduced. Both the etching reaction of Au and the *p*-nitrophenol reduction have


dx.doi.org/10.1021/jp5094433 | J. Phys. Chem. C 2014, 118, 28134–28142

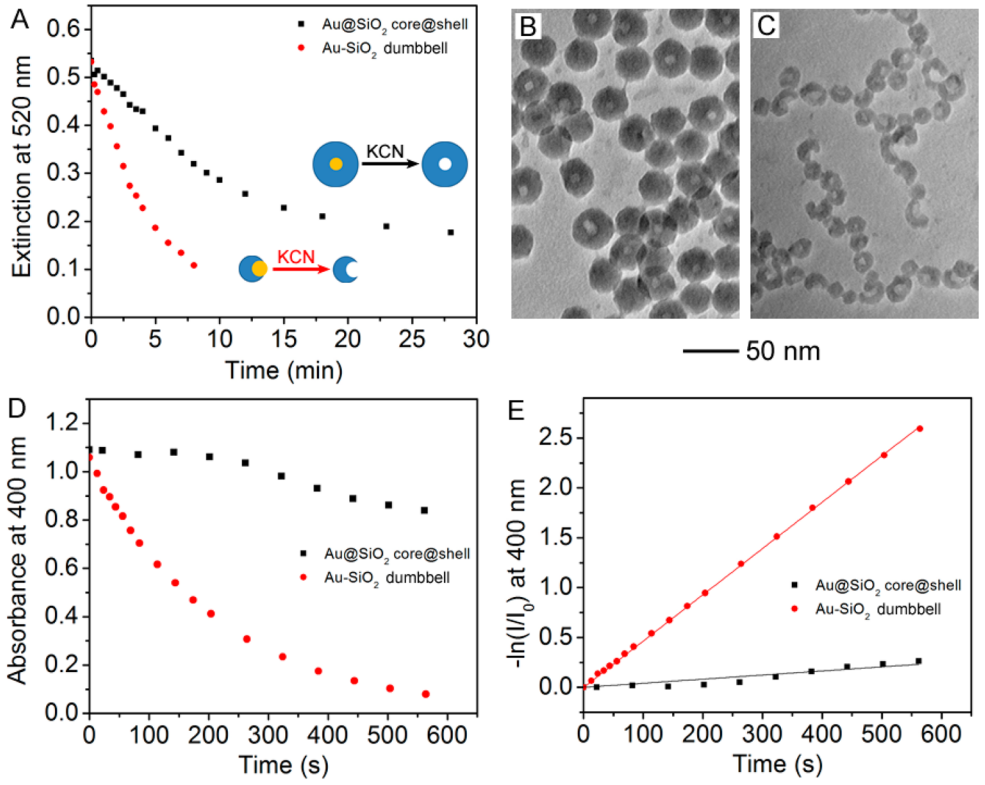


**Figure 7.** (A–C) Etching process of Au nanoparticles. (A) Plot of extinction at 520 nm as a function of etching time. (B, C) TEM images of Au@$SiO_2$ core@shell structures (B) and Au–$SiO_2$ dimers (C) after etching. (D, E) Kinetic study of 4-nitrophenol reduction on Au–$SiO_2$ nanostructures: (D) plot of normalized absorbance ($I/I_0$) of *p*-nitrophenolate ion at 400 nm as a function of time for different catalysts and (E) plot of $-\ln(I/I_0)$ as a function of time for different catalysts. Solid lines are linear fits of the data, and the slope gives $k_{app}$ of the reaction.

demonstrated that $SiO_2$ coating indeed serves as a mask to block chemical reactions.

## CONCLUSION

The MASG method has been developed with $SiO_2$ as a mask to partially protect the surface of seeds from further reaction and subsequently applied to synthesize Pd–Au and Pt–Au heterodimers and Pt–Pd–Au heterotrimers. The initial Au–$SiO_2$ dumbbell structures could be readily synthesized by a modified W/O microemulsion due to the phase separation of hydrophobic surface ligands and hydrophilic hydrolyzed TEOS. Further epitaxial growth of Pd and Pt on Au was observed. Interestingly, Pd is apt to laterally grow on Au by capping the unblocked Au surface, while Pt prefers to grow vertically into branched structures after initial deposition on Au. It is possible to replace the noble metal with a 3*d* transition metal as the second metal such that the active metal could subsequently be oxidized or sulfurized to oxide and sulfide.[52,53] Therefore, the MASG method is potentially a versatile strategy to generate hybrid heteronanostructures with multiple components for improving existing applications and finding new uses in many areas related to energy conversion and human health.

## ASSOCIATED CONTENT

### Supporting Information

Additional text with experimental details and eight figures showing TEM characterization of Au nanoparticles and Pt–Pd–Au heteronanostructures synthesized without protection of $SiO_2$, UV–vis spectra of Au nanoparticles and Au-$SiO_2$ dumbbells, and DDA simulations of optical spectra of individual Au-Pd dimers with different geometries and individual Au nanospheres with different diameters. This material is available free of charge via the Internet at http://pubs.acs.org.

## AUTHOR INFORMATION

### Corresponding Author

*E-mail chenj@uark.edu; phone +1 479-575-6203.

### Notes

The authors declare no competing financial interest.

## ACKNOWLEDGMENTS

This work was supported in part by the Ralph E. Powe Jr. Faculty Enhancement Award, funds from Arkansas Bioscience Institute, and startup funds from the University of Arkansas to J.C. The work done at Brookhaven National Laboratory was supported by the U.S. Department of Energy, Basic Energy Sciences, by the Materials Sciences and Engineering Division under Contract DE-AC02-98CH10886.

## REFERENCES

(1) Ferrando, R.; Jellinek, J.; Johnston, R. L. Nanoalloys: From Theory to Applications of Alloy Clusters and Nanoparticles. *Chem. Rev.* **2008**, *108*, 845–910.

(2) Zheng, H.; Li, Y.; Liu, H.; Yin, X.; Li, Y. Construction of Heterostructure Materials toward Functionality. *Chem. Soc. Rev.* **2011**, *40*, 4506–4524.

(3) Walther, A.; Müller, A. H. E. Janus Particles: Synthesis, Self-Assembly, Physical Properties, and Applications. *Chem. Rev.* **2013**, *113*, 5194–5261.

(4) Buck, M. R.; Schaak, R. E. Emerging Strategies for the Total Synthesis of Inorganic Nanostructures. *Angew. Chem., Int. Ed.* **2013**, *52*, 6154−6178.
(5) Liu, F.; Lee, J. Y.; Zhou, W. Template Preparation of Multisegment PtNi Nanorods as Methanol Electro-Oxidation Catalysts with Adjustable Bimetallic Pair Sites. *J. Phys. Chem. B* **2004**, *108*, 17959−17963.
(6) Liu, F.; Lee, J. Y.; Zhou, W. J. Multisegment PtRu Nanorods: Electrocatalysts with Adjustable Bimetallic Pair Sites. *Adv. Funct. Mater.* **2005**, *15*, 1459−1464.
(7) Paxton, W. F.; Kistler, K. C.; Olmeda, C. C.; Sen, A.; St. Angelo, S. K.; Cao, Y.; Mallouk, T. E.; Lammert, P. E.; Crespi, V. H. Catalytic Nanomotors: Autonomous Movement of Striped Nanorods. *J. Am. Chem. Soc.* **2004**, *126*, 13424−13431.
(8) Liu, R.; Sen, A. Autonomous Nanomotor Based on Copper−Platinum Segmented Nanobattery. *J. Am. Chem. Soc.* **2011**, *133*, 20064−20067.
(9) Salem, A. K.; Searson, P. C.; Leong, K. W. Multifunctional Nanorods for Gene Delivery. *Nat. Mater.* **2003**, *2*, 668−671.
(10) Park, S.; Son, Y. J.; Leong, K. W.; Yoo, H. S. Therapeutic Nanorods with Metallic Multi-Segments: Thermally Inducible Encapsulation of Doxorubicin for Anti-cancer Therapy. *Nano Today* **2012**, *7*, 76−84.
(11) Nicewarner-Peña, S. R.; Freeman, R. G.; Reiss, B. D.; He, L.; Peña, D. J.; Walton, I. D.; Cromer, R.; Keating, C. D.; Natan, M. J. Submicrometer Metallic Barcodes. *Science* **2001**, *294*, 137−141.
(12) Walton, I. D.; Norton, S. M.; Balasingham, A.; He, L.; Oviso, D. F.; Gupta, D.; Raju, P. A.; Natan, M. J.; Freeman, R. G. Particles for Multiplexed Analysis in Solution: Detection and Identification of Striped Metallic Particles Using Optical Microscopy. *Anal. Chem.* **2002**, *74*, 2240−2247.
(13) Al-Mawlawi, D.; Liu, C.; Moskovits, M. Nanowires Formed in Anodic Oxide Nanotemplates. *J. Mater. Res.* **1994**, *9*, 1014−1018.
(14) Hulteen, J. A General Template-based Method for the Preparation of Nanomaterials. *J. Mater. Chem.* **1997**, *7*, 1075−1087.
(15) Martin, B. R.; Dermody, D. J.; Reiss, B. D.; Fang, M.; Lyon, L. A.; Natan, M. J.; Mallouk, T. E. Orthogonal Self-Assembly on Colloidal Gold-Platinum Nanorods. *Adv. Mater.* **1999**, *11*, 1021−1025.
(16) Anderson, M. E.; Buck, M. R.; Sines, I. T.; Oyler, K. D.; Schaak, R. E. On-Wire Conversion Chemistry: Engineering Solid-State Complexity into Striped Metal Nanowires using Solution Chemistry Reactions. *J. Am. Chem. Soc.* **2008**, *130*, 14042−14043.
(17) Leonard, B. M.; Anderson, M. E.; Oyler, K. D.; Phan, T.-H.; Schaak, R. E. Orthogonal Reactivity of Metal and Multimetal Nanostructures for Selective, Stepwise, and Spatially-Controlled Solid-State Modification. *ACS Nano* **2009**, *3*, 940−948.
(18) Savas, T.; Schattenburg, M.; Carter, J.; Smith, H. I. Large-Area Achromatic Interferometric Lithography for 100 nm Period Gratings and Grids. *J. Vac. Sci. Technol., B: Microelectron. Nanometer Struct.–Process., Meas., Phenom.* **1996**, *14*, 4167−4170.
(19) Nikoobakht, B.; El-Sayed, M. A. Preparation and Growth Mechanism of Gold Nanorods (NRs) Using Seed-Mediated Growth Method. *Chem. Mater.* **2003**, *15*, 1957−1962.
(20) Gole, A.; Murphy, C. J. Seed-Mediated Synthesis of Gold Nanorods: Role of the Size and Nature of the Seed. *Chem. Mater.* **2004**, *16*, 3633−3640.
(21) Habas, S. E.; Lee, H.; Radmilovic, V.; Somorjai, G. A.; Yang, P. Shaping Binary Metal Nanocrystals through Epitaxial Seeded Growth. *Nat. Mater.* **2007**, *6*, 692−697.
(22) Lim, B.; Jiang, M.; Camargo, P. H.; Cho, E. C.; Tao, J.; Lu, X.; Zhu, Y.; Xia, Y. Pd-Pt Bimetallic Nanodendrites with High Activity for Oxygen Reduction. *Science* **2009**, *324*, 1302−1305.
(23) DeSantis, C. J.; Sue, A. C.; Bower, M. M.; Skrabalak, S. E. Seed-Mediated Co-reduction: A Versatile Route to Architecturally Controlled Bimetallic Nanostructures. *ACS Nano* **2012**, *6*, 2617−2628.
(24) Chen, S.; Jenkins, S. V.; Tao, J.; Zhu, Y.; Chen, J. Anisotropic Seeded Growth of Cu−M (M = Au, Pt, or Pd) Bimetallic Nanorods with Tunable Optical and Catalytic Properties. *J. Phys. Chem. C* **2013**, *117*, 8924−8932.
(25) Pellegrino, T.; Fiore, A.; Carlino, E.; Giannini, C.; Cozzoli, P. D.; Ciccarella, G.; Respaud, M.; Palmirotta, L.; Cingolani, R.; Manna, L. Heterodimers Based on $CoPt_3$−Au Nanocrystals with Tunable Domain Size. *J. Am. Chem. Soc.* **2006**, *128*, 6690−6698.
(26) Lim, B.; Kobayashi, H.; Yu, T.; Wang, J.; Kim, M. J.; Li, Z.-Y.; Rycenga, M.; Xia, Y. Synthesis of Pd−Au Bimetallic Nanocrystals via Controlled Overgrowth. *J. Am. Chem. Soc.* **2010**, *132*, 2506−2507.
(27) Zeng, J.; Zhu, C.; Tao, J.; Jin, M.; Zhang, H.; Li, Z. Y.; Zhu, Y.; Xia, Y. Controlling the Nucleation and Growth of Silver on Palladium Nanocubes by Manipulating the Reaction Kinetics. *Angew. Chem., Int. Ed.* **2012**, *51*, 2354−2358.
(28) Zhu, C.; Zeng, J.; Tao, J.; Johnson, M. C.; Schmidt-Krey, I.; Blubaugh, L.; Zhu, Y.; Gu, Z.; Xia, Y. Kinetically Controlled Overgrowth of Ag or Au on Pd Nanocrystal Seeds: From Hybrid Dimers to Nonconcentric and Concentric Bimetallic Nanocrystals. *J. Am. Chem. Soc.* **2012**, *134*, 15822−15831.
(29) Yang, Y.; Wang, W.; Li, X.; Chen, W.; Fan, N.; Zou, C.; Chen, X.; Xu, X.; Zhang, L.; Huang, S. Controlled Growth of Ag/Au Bimetallic Nanorods through Kinetics Control. *Chem. Mater.* **2012**, *25*, 34−41.
(30) Xie, S.; Peng, H.-C.; Lu, N.; Wang, J.; Kim, M. J.; Xie, Z.; Xia, Y. Confining the Nucleation and Overgrowth of Rh to the {111} Facets of Pd Nanocrystal Seeds: The Roles of Capping Agent and Surface Diffusion. *J. Am. Chem. Soc.* **2013**, *135*, 16658−16667.
(31) Chen, T.; Chen, G.; Xing, S.; Wu, T.; Chen, H. Scalable Routes to Janus Au−$SiO_2$ and Ternary Ag−Au−$SiO_2$ Nanoparticles. *Chem. Mater.* **2010**, *22*, 3826−3828.
(32) Ohmori, M.; Matijević, E. Preparation and Properties of Uniform Coated Inorganic Colloidal Particles: 8. Silica on Iron. *J. Colloid Interface Sci.* **1993**, *160*, 288−292.
(33) Liz-Marzán, L. M.; Philipse, A. P. Synthesis and Optical Properties of Gold-Labeled Silica Particles. *J. Colloid Interface Sci.* **1995**, *176*, 459−466.
(34) Roca, M.; Haes, A. J. Silica−Void−Gold Nanoparticles: Temporally Stable Surface-Enhanced Raman Scattering Substrates. *J. Am. Chem. Soc.* **2008**, *130*, 14273−14279.
(35) Guerrero-Martínez, A.; Pérez-Juste, J.; Liz-Marzán, L. M. Recent Progress on Silica Coating of Nanoparticles and Related Nanomaterials. *Adv. Mater.* **2010**, *22*, 1182−1195.
(36) Johnson, C. L.; Snoeck, E.; Ezcurdia, M.; Rodriguez-Gonzalez, B.; Pastoriza-Santos, I.; Liz-Marzan, L. M.; Hytch, M. J. Effects of Elastic Anisotropy on Strain Distributions in Decahedral Gold Nanoparticles. *Nat. Mater.* **2008**, *7*, 120−124.
(37) Jungjohann, K. L.; Bliznakov, S.; Sutter, P. W.; Stach, E. A.; Sutter, E. A. In Situ Liquid Cell Electron Microscopy of the Solution Growth of Au−Pd Core−Shell Nanostructures. *Nano Lett.* **2013**, *13*, 2964−2970.
(38) Kibler, L. A.; Kleinert, M.; Randler, R.; Kolb, D. M. Initial Stages of Pd Deposition on Au(hkl) Part I: Pd on Au(111). *Surf. Sci.* **1999**, *443*, 19−30.
(39) Naohara, H.; Ye, S.; Uosaki, K. Electrochemical Layer-by-Layer Growth of Palladium on an Au(111) Electrode Surface: Evidence for Important Role of Adsorbed Pd Complex. *J. Phys. Chem. B* **1998**, *102*, 4366−4373.
(40) Ding, Y.; Fan, F.; Tian, Z.; Wang, Z. L. Atomic Structure of Au−Pd Bimetallic Alloyed Nanoparticles. *J. Am. Chem. Soc.* **2010**, *132*, 12480−12486.
(41) Koel, B. E.; Sellidj, A.; Paffett, M. T. Ultrathin Films of Pd on Au(111): Evidence for Surface Alloy Formation. *Phys. Rev. B* **1992**, *46*, 7846−7856.
(42) Shibata, T.; Bunker, B. A.; Zhang, Z.; Meisel, D.; Vardeman, C. F.; Gezelter, J. D. Size-Dependent Spontaneous Alloying of Au−Ag Nanoparticles. *J. Am. Chem. Soc.* **2002**, *124*, 11989−11996.
(43) Langhammer, C.; Yuan, Z.; Zoric, I.; Kasemo, B. Plasmonic Properties of Supported Pt and Pd Nanostructures. *Nano Lett.* **2006**, *6*, 833−838.
(44) Draine, B. T.; Flatau, P. J. Discrete-Dipole Approximation for Scattering Calculations. *J. Opt. Soc. Am. A* **1994**, *11*, 1491−1499.

(45) Liao, H.-G.; Cui, L.; Whitelam, S.; Zheng, H. Real-time Imaging of $Pt_3Fe$ Nanorod Growth in Solution. *Science* **2012**, *336*, 1011−1014.
(46) Li, D.; Nielsen, M. H.; Lee, J. R.; Frandsen, C.; Banfield, J. F.; De Yoreo, J. J. Direction-specific Interactions Control Crystal Growth by Oriented Attachment. *Science* **2012**, *336*, 1014−1018.
(47) Waibel, H.-F.; Kleinert, M.; Kibler, L.; Kolb, D. Initial Stages of Pt Deposition on Au (111) and Au (100). *Electrochim. Acta* **2002**, *47*, 1461−1467.
(48) Sanchez, S. I.; Small, M. W.; Zuo, J.-m.; Nuzzo, R. G. Structural Characterization of Pt−Pd and Pd−Pt Core−Shell Nanoclusters at Atomic Resolution. *J. Am. Chem. Soc.* **2009**, *131*, 8683−8689.
(49) Koole, R.; van Schooneveld, M. M.; Hilhorst, J.; de Mello Donegá, C.; Hart, D. C.; van Blaaderen, A.; Vanmaekelbergh, D.; Meijerink, A. On the Incorporation Mechanism of Hydrophobic Quantum Dots in Silica Spheres by a Reverse Microemulsion Method. *Chem. Mater.* **2008**, *20*, 2503−2512.
(50) Park, S.-J.; Kim, Y.-J.; Park, S.-J. Size-Dependent Shape Evolution of Silica Nanoparticles into Hollow Structures. *Langmuir* **2008**, *24*, 12134−12137.
(51) Herves, P.; Pérez-Lorenzo, M.; Liz-Marzán, L. M.; Dzubiella, J.; Lu, Y.; Ballauff, M. Catalysis by Metallic Nanoparticles in Aqueous Solution: Model Reactions. *Chem. Soc. Rev.* **2012**, *41*, 5577−5587.
(52) Hung, L.-I.; Tsung, C.-K.; Huang, W.; Yang, P. Room-Temperature Formation of Hollow $Cu_2O$ Nanoparticles. *Adv. Mater.* **2010**, *22*, 1910−1914.
(53) Motl, N. E.; Bondi, J. F.; Schaak, R. E. Synthesis of Colloidal Au−$Cu_2S$ Heterodimers via Chemically Triggered Phase Segregation of AuCu Nanoparticles. *Chem. Mater.* **2012**, *24*, 1552−1554.